Oxygen-driven de-alloying of Fe-14Cr-12Ni-10Mn-3Cu-2.5Al-1Nb austenitic steel at 500 °C in static Pb-Bi eutectic with concentration of dissolved oxygen alternating from 10^{-6} to 10^{-9} mass% for 10000 h

Tsisar, Valentyn; Stergar, Erich; Gavrilov, Serguei; Maia, Eloa Lopes; Van Renterghem, Wouter; Louette, Pierre; Lucas, Stéphane

Published in:
Corrosion Communication

DOI:
10.1016/j.corcom.2024.01.002

Publication date:
2025

Document Version
Publisher's PDF, also known as Version of record

Corrosion Communications 17 (2025) 1–11

Contents lists available at ScienceDirect

Corrosion Communications

journal homepage: www.elsevier.com/locate/corcom

Research Article

Oxygen-driven de-alloying of Fe-14Cr-12Ni-10Mn-3Cu-2.5Al-1Nb austenitic steel at 500 °C in static Pb-Bi eutectic with concentration of dissolved oxygen alternating from ~10^{-6} to 10^{-9} mass% for 10000 h

Valentyn Tsisar[a,*], Erich Stergar[a], Serguei Gavrilov[a], Eloa Lopes Maia[a,b], Wouter Van Renterghem[a], Pierre Louette[c], Stéphane Lucas[c]

[a] Belgian Nuclear Research Centre SCK•CEN, Boeretang 200, Mol B-2400, Belgium
[b] Vrije Universiteit Brussel (VUB), Electrochemical and Surface Engineering (SURF), Pleinlaan 2, B-1050, Brussel, Belgium
[c] University of Namur, Rue de Bruxelles, 61, B-5000 Namur, Belgium

ARTICLE INFO

Article history:
Received 31 October 2023
Received in revised form 21 December 2023
Accepted 12 January 2024

Keywords:
Austenitic stainless steel
Corrosion
De-alloying
Liquid lead-bismuth eutectic
Oxidation

ABSTRACT

A high-Mn austenitic steel Fe-14Cr-12Ni-10Mn-3Cu-2.5Al-1Nb was tested at 500 °C in static Pb-Bi eutectic for 10000 h. In the course of the test, oxygen concentration in liquid metal was cycled from ~10^{-6} to ~10^{-9} mass%, which provides oxidation and dissolution regimes, respectively. After 10000 h exposure steel showed formation of ferrite corrosion zone depleted in Mn, Ni, Cu, Cr, Fe and penetrated by Pb and Bi. Average depth of corrosion is 15±5 μm, while maximum corrosion depth locally reaches ~35 μm. Dissolved Mn and Cr re-precipitated in the vicinity of steel surface in a form of stratified Mn-O/Cr-Mn-O oxide scale. Obtained results were compared to those of similar Al-alloyed austenitic steels with lower Mn content, which exhibited protective oxidation under same test conditions. The phenomenological mechanism of oxygen-driven de-alloying of steel in Pb-Bi[O] is discussed.

1. Introduction

Corrosion issues of steels in Pb-based liquid metals such as Pb, Pb-Bi and Pb-Li eutectics represent a crucial obstacle to the development and implementation of high-temperature energetic nuclear and non-nuclear installations. A number of reviews have outlined the main phenomena that occur in solid metal/liquid metal systems [1–6]. These include dissolution - a fundamental interaction phenomenon between solid and liquid metals and in-situ oxidation. The latter is considered as a main dissolution mitigation technique which involves controlled addition and monitoring of oxygen impurity levels in lead-based liquid metals such as Pb and Pb-Bi eutectic [7]. The durability of in-situ formed Fe-Cr oxide layers on the surfaces of austenitic steels 316 L and 1.4970 plays a crucial role in mitigating liquid-metal corrosion [8]. As the protective properties of these in-situ Fe-Cr oxide layers locally degrade, the primary steel constituents (Ni, Cr, Fe) leach, causing phase transformations within corrosion zone from austenite to ferrite and liquid metal infiltration into solid [8]. Based on the corrosion data obtained in several long-term experimental campaigns [8–12], it is believed that temperature limit for austenitic steels should not exceed 400–480 °C providing that proper oxygen control in liquid metal is ensured. For high operation temperatures, one should consider protective coatings or new materials.

Austenitic steels alloyed with aluminium can improve their corrosion resistance in lead-based liquid metals by forming a continuous and protective alumina scale, potentially increasing operation temperatures. These steels are designated as Alumina-Forming Austenitic steels (AFA) in literature [13–15]. Concentration of aluminium in these types of austenitic steels ranges from 2.4% to 4.1% (mass fraction) [16]. It is adequate for the formation of a continuous and protective alumina film in gaseous environments at temperatures above 650 °C [17]. However, the formation of Al-based oxide films on the surface of AFA steels in-situ in lead-based liquid metals can be challenging, because the operating temperatures for austenitic stainless steels in contact with lead-based melts are typically limited to ≤ 480 °C that is low enough for the active diffusion of Al (strong α-ferrite stabilizer) in the austenitic matrix. In addition, the working concentration of oxygen in the lead-based melts should be maintained at a comparably high level,

* Corresponding author.
E-mail address: valentyn.tsisar@sckcen.be (V. Tsisar).

https://doi.org/10.1016/j.corcom.2024.01.002

i.e.: $C_{O[Pb,\ Pb\text{-}Bi]} \geq C_{O[Fe(s)/Fe_3O_4(s)]}$, which involves the main steel constituents such as Fe, Cr, Si and Mn in the oxidation process [18].

Several experimental works already demonstrated that AFA steels show very good corrosion resistance at 550–600 °C in lead-based (Pb, Pb-Bi eutectic) static and flowing liquid metals when the concentration of dissolved oxygen is controlled above the thermodynamic stability of magnetite, i.e.: ~10^{-7} – 10^{-6} mass% [19–21]. This was attributed to the formation of thin and protective alumina-rich oxide films. Chromium, similar to gaseous oxidation, has a beneficial effect in reducing the required aluminum concentration in the steels to form protective alumina-rich films, known as the third element effect [22]. Nickel generally does not participate in oxidation processes in lead-based melts because the "working" concentration of oxygen in liquid metals is lower than that required to form NiO [23].

In this paper, we are presenting and discussing the experimental results on the corrosion behavior of a high-Mn Al-alloyed austenitic steel Fe-14Cr-12Ni-10Mn-3Cu-2.5Al-1Nb in Pb-Bi eutectic at 500 °C. Manganese is an austenite stabilizer and is used in austenitic steels as a partial substitute for Ni. With respect to oxidation, Mn, similar to Cr, has a much higher affinity for oxygen than Ni and can therefore actively participate in the formation of oxide layers. At the same time, it has a high solubility in lead-based melts, which is quantitatively similar to Ni [3]. Manganese reduces the oxidation resistance of steels and alloys in gaseous environments [24–27]. The negative effect of high Mn content (15 wt.%) in the alloys on oxidation resistance is manifested in the formation of coarse Mn-rich oxide nodules and spallation of the scale, leading to mass loss [26].

In contrast to gaseous oxidation, little work has been done to elucidate the corrosion behavior of Mn-alloyed steels in lead-based liquids. In oxygen-saturated liquid Pb-Bi, a multilayer non-protective scale (12.5 μm) was formed on the surface of high-Mn austenitic steels (mass%: Fe-21Mn-(4.9-7)Al-1Cr-(0.4-0.8)C) at 450 °C for 430 h [28]. In Pb-Bi with “low” oxygen concentrations (1.6×10^{-8} – 6.0×10^{-10} mass%), a duplex scale layer (3 μm) consisting of an outer Mn-Fe-rich oxide and an inner Al-rich oxide scale was formed and considered by the authors as a protective scale. Corrosion resistance improved with increasing Al content in these steels [28]. Oxide dispersion-strengthened (ODS, $YAlO_3$) Al-added high-Mn austenitic steels showed superior oxidation resistance over conventional steel of the same composition in oxygen-saturated Pb-Bi at 450 °C for 430 h due to the formation of internal continuous Al-rich oxide layer as a result of fine-grained structure of ODS steel with high-density of diffusion paths [29]. In these cases, the inner Al-rich oxide layer plays the role of a mass transfer barrier, inhibiting the redistribution of reactants between the steel and the molten metal. A similar interaction is observed in Si-alloyed steels, where Si oxidizes internally, slowing the overall oxidation rate but not changing the morphology of the oxide layers, which generally remain bilayer [30,31].

Recently Pint and coauthors performed an initial evaluation of the corrosion behavior of a family of AFA steels (mass%) Fe-(14-16)Cr-(8-25)Ni-(1.9-4.8)Mn-(2.3-3.9)Al-3Cu-(0.13-0.16)Si-(0.6-1.4)Nb moderately alloyed by Mn in static and flowing Pb at 500–800 °C [32]. In static Pb under dissolving conditions, the AFA steels showed only at 600 °C lower mass changes than the reference 316H steel. However, at higher temperatures, the AFA steels showed even higher corrosion losses. In flowing Pb with higher oxidation potential after 1000 h exposure at 550–650 °C, AFA steels showed limited signs of corrosion accompanied by relatively low mass changes while 316H steel showed accelerated oxidation forming a thick duplex Fe-rich oxide scale [32].

In our previous publication, we characterized AFA steels alloyed with moderate amounts of Mn (2 mass%–5 mass%) as potential materials for use in contact with Pb-Bi eutectic at 500 °C. This is due to the high durability of the in-situ formed oxide films [33]. In contrast, a high-Mn (10 mass%) Al-alloyed austenitic steel, subjected to the same experimental conditions, resulted in dissolution corrosion (the present study). The variety of the corrosion interactions observed between the high-Mn AFA steel and the liquid Pb-Bi eutectic prompted us to provide a comprehensive analysis of the observed phenomena in this article.

2. Experimental

A high-Mn Al-alloyed Fe-14Cr-12Ni-10Mn-3Cu-2.5Al-1Nb austenitic steel was supplied by Oak Ridge National Laboratory in view of 15 mm thick plate after solution annealing at 1200 °C for 0.25–0.5 h and water quenching [16]. The composition (mass fraction, %) of steel is Cr 13.89, Ni 12.09, Mn 9.96, Cu 3.06, Al 2.54, Si 0.14, Nb 1.01, V 0.05, Ti 0.05, Mo 0.15, W 0.15, C 0.200, B 0.009, N 0.0044, P 0.024, S 0.0010, Fe Bal. Alloying with Mn reduces steel costs and stabilizes single-phase austenitic matrix at a given level of Ni, while the content of ferrite stabilizing Al and Cr should provide the formation of protective Al-based oxide film. MC-base precipitates (M=Nb), $M_{23}C_6$ (M=Cr, Nb) and γ'-Ni_3Al precipitates ensure creep strength [16].

Cylindrical specimens (Ø5 mm × 100 mm) were fabricated by spark erosion, followed by turning as the final manufacturing step. Surface roughness parameters of samples are as follows: R_a=0.4055 μm; R_q=0.5174 μm; R_t=3.4536 μm and R_z=2.9573 μm.

Fig. 1(a) shows microstructure of steel obtained from the area of 895 μm × 665 μm on the transversal metallographic cross-section with an aid of scanning electron microscopy based electron back scatter diffraction (SEM-EBSD, Jeol JSM6610LV) in combination with a Bruker (XFLASH 4010) energy dispersive X-ray (EDX) detector and electron backscatter diffraction (EBSD) high-resolution eFlash^{HR} detector. The pattern quality map is overlapped with grain boundaries map (Fig. 1(a)). Grain size distribution was analyzed based on about 900 grains (excluding twin boundaries) and ranges from several microns to about 115 μm in diameter with the largest fraction between 25 and 80 μm and averages of 53 μm (Fig. 1(b)). The total length of characterized boundaries (including twin boundaries) reaches about 100 mm. The high-angle random boundaries are colored in white and coincidence site lattice (CSL) boundaries are colored in blue and green in Fig. 1(a). CLS boundaries compose of 58% of boundaries. Most of CSL boundaries are twin boundaries (Σ3, ⟨111⟩, 60°). Nb(Ti) plate-like primary carbides are detected in the composition of steel in the form of bands precipitated along rolling direction (Fig. 1(c, d)).

Fig. 2 shows a schematic diagram of the experimental setup for static corrosion tests consisting of a stainless steel autoclave with a lid. It has connections for gas inlet and outlet (Ar, Ar-5%H_2, air), thermocouple, sample holder, oxygen pump [34] and Bi/Bi_2O_3 electrochemical oxygen sensor [35,36]. The autoclave resides an alumina crucible filled with 5 kg of fresh liquid Pb-Bi eutectic. The molten metal was preconditioned with respect to temperature (500 °C) and initial oxygen concentration (~10^{-6} mass%) prior to the introduction of the sample. The ratio between the volume of liquid metal (cm^3) and the surface of samples (cm^2) is 1.7 cm.

Test was carried out at 500 ± 2 °C in a static Pb-Bi eutectic with a purposeful variation of the oxygen concentration from about ~10^{-6} to ~10^{-9} mass% for 10000 h (Fig. 3).

The test conditions were selected to explore the potential for in-situ formation of protective oxide layers on the surface of Al-alloyed austenitic steels in static Pb-Bi eutectic at elevated temperature (500 °C). The study is aimed to demonstrate the long-term (10000 h) durability of the formed barriers under variations in oxygen concentration in the liquid metal. This experiment simulates transient accidental interruptions of the oxygen supply to the system, which can cause a drop in oxygen concentration and lead to undesirable dissolution-controlled corrosion. In this work, we conducted a test lasting 10000 h, which is a comparably long-term test for the laboratory experiments. This duration is more representative of assessing the lifetime of replaceable components, such as cladding tubes, in liquid-metal cooled reactors, which are expected to operate for several decades.

The experiment is divided into two main domains with respect to oxygen concentration in liquid Pb-Bi: domain 1) provides oxidizing con-

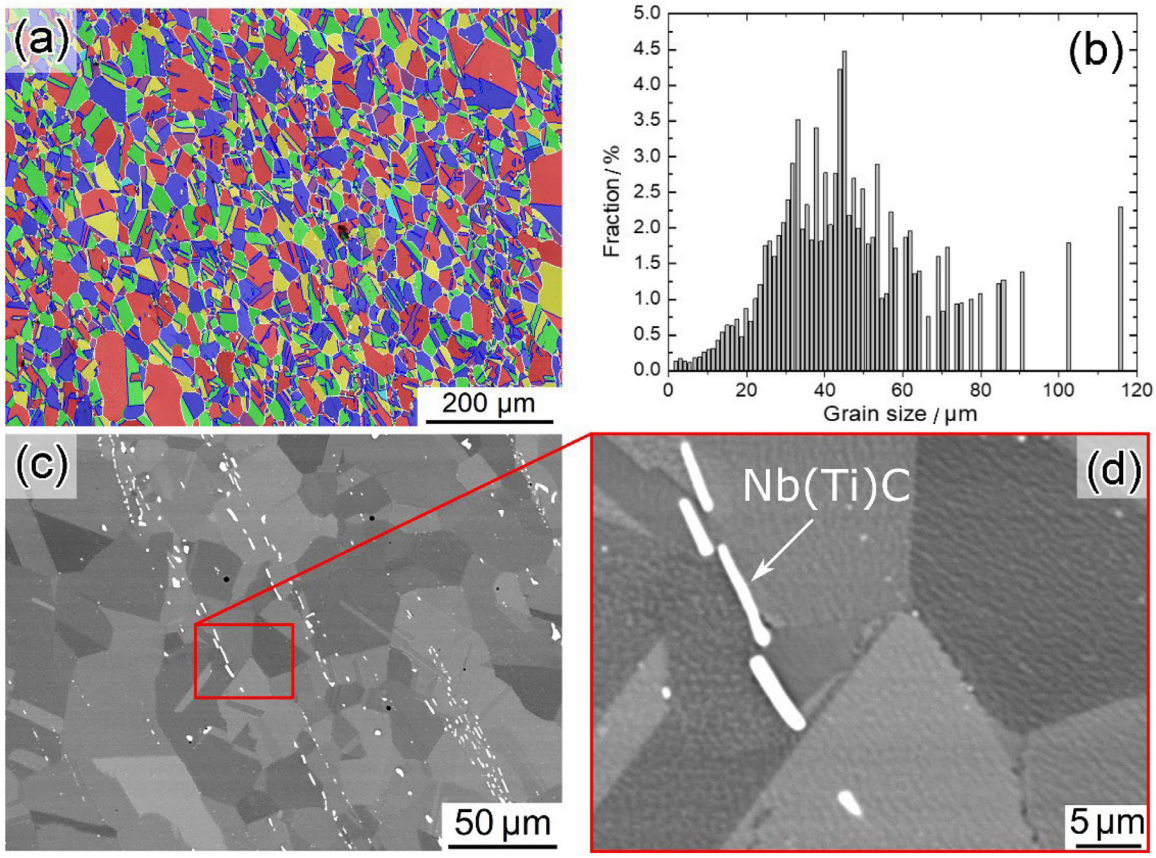

Fig. 1. Structure of Fe-14Cr-12Ni-10Mn-3Cu-2.5Al-1Nb steel in as-received annealed state: (a) EBSD pattern quality map overlapped with grain-boundary map shows white-colored high-angle boundaries; blue-colored twin boundaries (Σ3, ⟨111⟩, 60°) and green-colored - CSL boundaries (Σ9, ⟨110⟩, 38.94°); (b) grain size distribution; back-scattered electron micrographs showing (c) precipitation bands and (d) individual precipitates of Nb(Ti)C carbides in steel matrix, respectively.

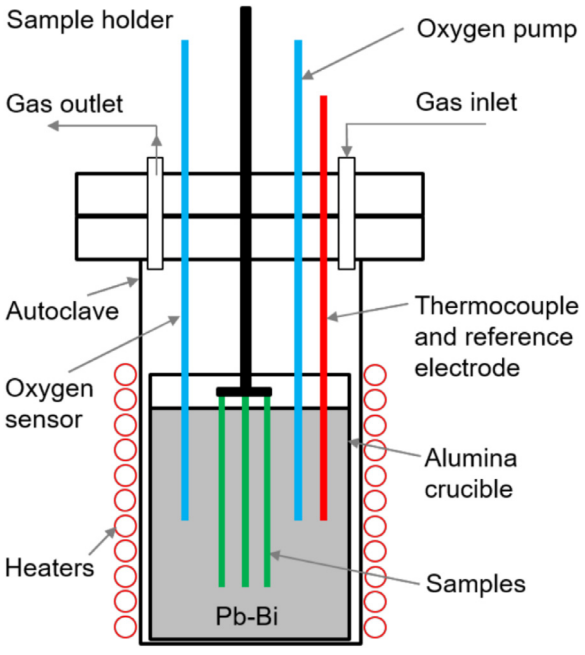

Fig. 2. Principal scheme of apparatus for corrosion tests in static Pb-Bi eutectic.

ditions - the oxygen concentration is maintained at ~10^{-6} mass% which should ensure in-situ formation of oxide layer on steel surface and domain 2) which provides dissolution conditions – oxygen concentration is maintained at ~10^{-9} mass% which might destabilize magnetite (Fe_3O_4) while the Cr-, Mn-, and Al-based oxides are remain stable at least thermodynamically (Fig. 3). Oxidizing domain is first in order to provide initial oxidation since in our previous work Al-alloyed steel showed oxidation only when the oxygen concentration was maintained at ~10^{-6} mass% at 550 °C ($C_{O[Pb\text{-}Bi]} \geq C_{O[Fe(s)/Fe_3O_4(s)]}$) while at lower oxygen concentrations ($C_{O[Pb\text{-}Bi]} \leq C_{O[Fe(s)/Fe_3O_4(s)]}$) AFA steels showed dissolution corrosion in-spite of the fact that these concentrations ensured thermodynamic stability of alumina and chromia [18].

The test conditions change throughout the testing process (Fig. 3), beginning with oxidation (1100 h), then transitioning to dissolution (500 h), followed by a return to oxidation (3600 h), transitioning again to dissolution (1200 h), and finally returning to oxidation (3600 h).

After a 10000 h exposure, the samples were extracted from the liquid Pb-Bi and segmented through mechanical cutting. The segment for surface examination underwent a cleaning process to remove solidified Pb-Bi. It was initially cleaned in hot glycerin at about 150 °C, degreased in ethanol, and subsequently chemically cleaned in a 1:1:1 mixture of acetic acid (CH_3COOH), hydrogen peroxide (H_2O_2), and ethanol (C_2H_5OH) at room temperature. A segment with adhered Pb-Bi was used for cross-sectional analysis. Seven cross-sections were prepared and analyzed to represent the corrosion appearances along the height of the sample.

Corrosion depth of the samples was assessed using light optical microscopy (LOM). Detailed high resolution image of the cross-section was captured using image stitching techniques (Fig. 4). A routine procedure was employed to measure the corrosion depth. The process includes reconstructing the original diameter of the sample by utilizing corrosion-free regions of the sample surface, detecting the center, and measuring the corrosion depth relative to the reconstructed circle every

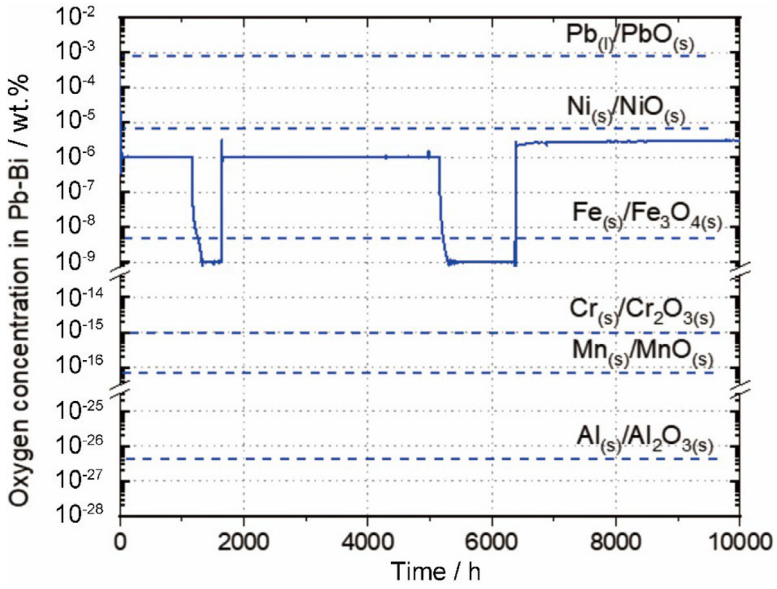

Fig. 3. Time dependence of oxygen concentration in liquid Pb-Bi during the experiment. Blue dashed horizontal lines indicate the concentrations of oxygen which correspond to the thermodynamic equilibrium between Me/Me_xO_y (Me = Pb, Ni, Fe, Cr, Mn and Al).

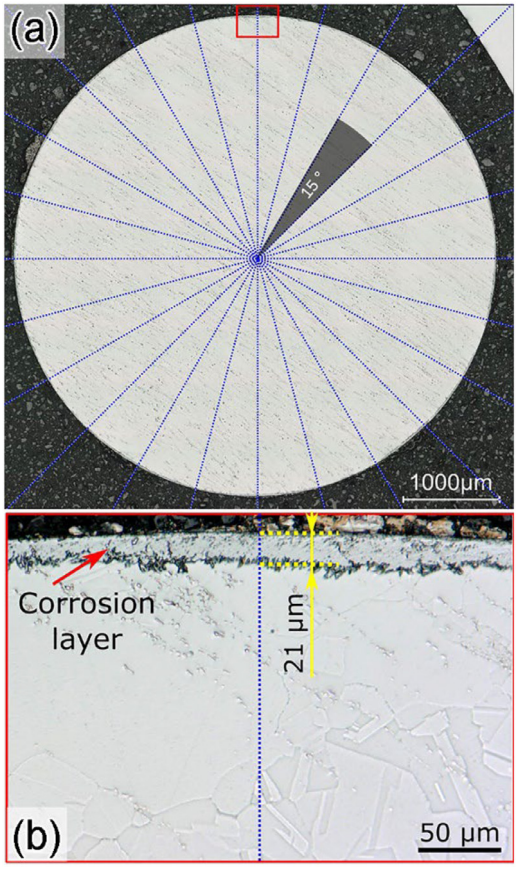

Fig. 4. Example of methodology for measuring the thickness of corrosion layer along the circumference of cross-section obtained by light optical microscopy: (a) sample cross-section overlapped by the dotted assisting lines with the 15° step, (b) example of corrosion depth measurements along the assisting dotted line.

15° along the guidelines (Fig. 4(a)). Regular 24 measurements per one cross-section were carried out to obtain the corrosion depth (Fig. 4(b)). Additionally, the metallographic cross-section was examined along the circumference to determine the maximum corrosion depth, which may not have been obtained from the regular measurements. The percentage of corrosion coverage for a given sample was determined by observing 24 regularly spaced cross-sections near a guideline that crosses the interface between the steel surface and the solidified Pb-Bi. The obtained results were statistically elaborated and the corrosion data are presented as the average value of corrosion depth with standard deviations, maximum value and percentage of surface showing corrosion.

Digital light-optical microscopes Keyence VHX6000 and Alicona InfiniteFocusSL were used to observe 3D surface microscopy and metrology, as well as 2D cross-sectional metallography of samples. Morphology, microstructure and elemental composition of corrosion zones were determined using SEM in combination with EDX detector and EBSD detector. Thermo Fisher Scios, which combines the FEG-SEM with a 30 kV Ga^+ ion beam (Dual-Beam focused ion beam: DB-FIB) was used to mill local cross-sections directly from the samples surface areas of interest. X-ray photoelectron spectroscopy (XPS, Thermo Scientific™ K-Alpha™ X-ray Photoelectron Spectrometer System) was used to analyze composition and oxidation states of elements in the oxide films formed.

3. Results

3.1. Surface examination

Cleaned sample surface, formerly covered by solidified Pb-Bi, exhibited slight oxidation as evidenced by a change in color from its original metallic luster to a matte blue hue (Fig. 5). Additionally, the surface is noticeably populated with hemispherical pits in various sizes (Fig. 5(a, b)). The morphology of the pit mouth appears spongy in nature (Fig. 6(a)). The surface EDX analyses indicate a significant depletion of Ni, Mn, and Cu in comparison to the initial steel composition (Fig. 6(b), area A). The adjacent areas of the pit share a similar composition (Fig. 6(b), area B), albeit showing slight oxidation. The presence of Bi in area B's composition may be explained by the oxide film protective action that prevents Bi and Pb from completely cleaning from the sub-oxide zone. This is in contrast to the unprotected surface of the pit in area A.

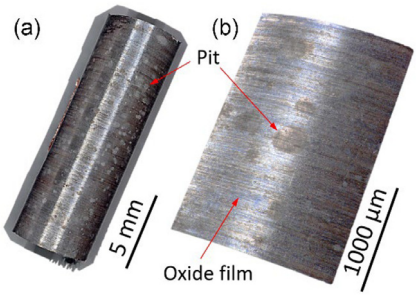

Fig. 5. Surface of the Fe-14Cr-12Ni-10Mn-3Cu-2.5Al-1Nb corrosion sample after exposure at 500 °C to static Pb-Bi for 10000 h: (a) three-dimensional overview of the corrosion sample, (b) detail out of Fig. 5(a) with higher magnification. Sample is cleaned chemically with respect to solidified Pb-Bi.

XPS spectra accompanied by intensity contour maps of Fe, Cr, Ni, Mn, Al, O, Pb and Bi are shown in Fig. 7. The high resolution spectra are obtained by sputtering to a depth marked as the etch levels from # 0 to # 100. The Fe $2p_{3/2}$ spectra revealed small surface peaks around 710 eV which could be associated with the magnetite. The metallic Fe with a binding energy of 706.8 eV appeared in deeper layers (Fig. 7(a)). The small peaks of Cr $2p_{3/2}$ at 577.2 eV are consistent with the mixed chromium oxide detected at the surface up to etching level # 25 (Fig. 7(b)) [37]. With increasing etching depth the peaks of metallic Cr at 574.3 eV become dominant. The only peaks of metallic Ni are detected at a binding energy of 852.8 eV starting at the etching level # 75 (Fig. 7(c)). The Mn $2p_{3/2}$ spectra and corresponding intensity contour-map imply the formation of a Mn-containing oxide on the surface and a bit deeper near-surface layers with binding energies of 641.9 and 641.3 eV, respectively (Fig. 7(d)). Metallic Mn (638.7 eV) is not detected until the deepest levels of etching. The weak signals at 74.9 eV (near surface) and 75 eV (deeper layers) correspond to Al oxides while a peak indicating metallic Al (72.8 eV) is not found (Fig. 7(e)). O 1s spectra are detected until the deepest etch level although the corresponding intensity contour-map clearly reveals oxygen only at the surface (Fig. 7(f)). The binding energies at 531–532.3 eV are usually associated with the formation of defected spinel-type oxides or organic compounds [38,39]. In spite of surface cleaning clear peaks of Pb 4f and Bi 4f are observed in the XPS spectra (Fig. 7(g, h)). It is interesting to notice that based on the intensity contour-maps Pb (139.3 and 144.3 eV) and Bi (160.0 and 165.2 eV) oxides accumulate preferentially close to the surface, while metallic Bi (157.2 and 162.3 eV) is detected preferentially in the deeper layers of material. Formation of Pb and Bi oxides is not expected in our test conditions according to the thermodynamic evaluations (Fig. 3). Therefore one can assume that the cleaning procedure might result in the oxidation of Pb and Bi remaining in corrosion layer. Separation of Pb and Bi eutectic near the oxidation-corrosion zones was already reported and explained by preferential oxidation of Pb which might participate in the formation of more complex oxides $Pb_xFe_yO_z$ while more "noble" Bi penetrates deeper into the corrosion zone [40].

Based on the XPS spectra and intensity contour maps, the thin oxide film could be identified as a mixture of $(Mn\text{-}Fe\text{-}Al\text{-}Cr)_xO_y$ compounds.

3.2. Cross-sectional examinations

Cross-sectional examinations revealed the formation of a uniform corrosion layer with an average thickness of 15±4.2 µm (Fig. 8(a)). The maximal depth reaches locally, about 34.6 µm (Fig. 8(b)). The corrosion layer covers approximately 80% of the surface. Based on backscattered electron image atomic contrast (Fig. 8) and EDX analyses along the horizontal dotted line identified in Fig. 9(a), the corrosion layer is substantially depleted in Mn, Cu and to a lesser extent in Ni when compared to un-corroded steel bulk (Fig. 9(b)). The corrosion zone is also markedly penetrated by Pb and Bi.

Fig. 10 shows EBSD maps of the corrosion and sub-corrosion zones of the sample. The pattern quality (PQ) and inverse pole figures (IPF-Z) maps illustrate a very fine-grained corrosion layer (Fig. 10(a, b)). According to the phase distribution (PD) map in Fig. 10(c), the corrosion layer is composed of ferrite. This suggests that the leaching of austenite stabilizers (Mn and Ni) by liquid metal caused the phase transformation of near-surface zones of steel from austenite to ferrite. The grain average misorientation (GAM) map in Fig. 10(d) shows an accumulation of deformation in the near-surface zone of the sample to the depth about 20 µm as a change in orientation from 0° (blue) to 5° (red). This is a result of the preparation of rod samples by turning. The stored deformation was not released by long-term aging at 500 °C for 10000 h. However, the corrosion-induced phase transformation released the stored deformation in the corrosion layer at the top of the deformed zone (Fig. 10(c, d)).

Fig. 11 shows two examples of oxide scales that were sporadically observed on the original steel surface. Thickness of the denser outer layer and looser inner layer average 14.1±2.9 and 22.1±6.4 µm, respectively. The outer oxide is composed of Mn and O with proportions of 45% and 55% (at.%), respectively, as analyzed by EDX, while the inner oxide with a composition of Cr-Mn-O (at.%: 26-16-58) was infiltrated by Pb and Bi (Fig. 11(d, f)). Iron and nickel are not present in the composition of oxide agglomerates.

Despite the prevalence of dissolution corrosion, approximately 20% of the sample surface remains uncorroded. Fig. 12 depicts the overall (Fig. 12(a)) and detailed (Fig. 12(b, d)) structure of the near-surface zone that has remained corrosion-free. The zone can be divided into three subzones starting from the surface: 1) a top layer approximately 5 µm thick that has a nano-grained structure, 2) an intermediate layer 20-25 µm thick featuring deformation bands, and 3) the annealing twins of the solutionized steel bulk (Fig. 12(a, b)). As it was already mentioned above, it has been formed due to surface deformation that occurs during the manufacturing process via turning. A peak-like redistribution of steel components (Cr, Fe, Ni, Mn, Cu) is observed in sub-surface regions as

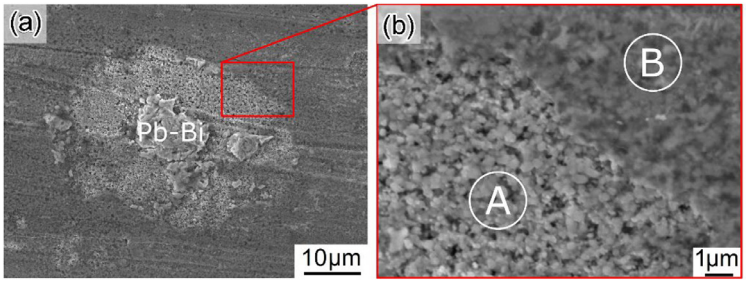

wt.%	Steel	A	B
Fe	Balance		
Cr	14	17	15
Ni	12	3	4
Mn	10	2	3
Cu	3	0	0.3
Al	2.5	0.5	4
Bi	-	5	11
O	-	-	7.1

Fig. 6. Pit-type corrosion damage formed on the surface of the Fe-14Cr-12Ni-10Mn-3Cu-2.5Al-1Nb steel during exposure at 500 °C to static Pb-Bi for 10000 h: (a) general view, (b) detailed view of transient zone between surface of pit and "original" surface of steel accompanied by compositions obtained by EDX spot analyses in zone of pit (A) and on "original" surface of steel. Sample is cleaned chemically with respect to solidified Pb-Bi.

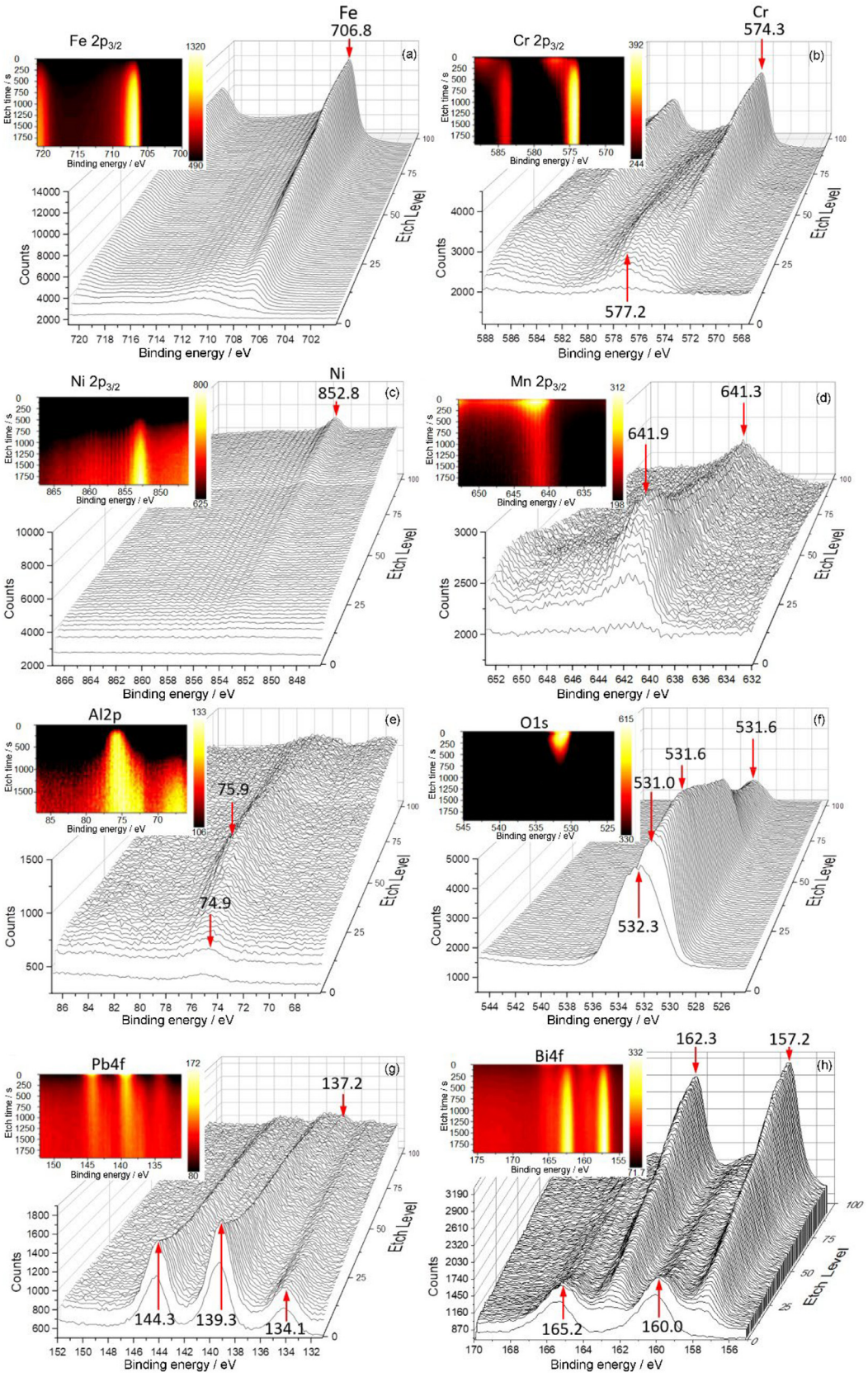

Fig. 7. XPS spectra of (a) Fe $2p_{3/2}$, (b) Cr $2p_{3/2}$, (c) Ni $2p_{3/2}$, (d) Mn $2p_{3/2}$, (e) Al 2p, (f) O 1 s, (g) Pb 4f and (h) Bi 4f accompanied by intensity contour maps as function of etching time obtained from the surface of the investigated Fe-14Cr-12Ni-10Mn-3Cu-2.5Al-1Nb steel exposed at 500 °C in static Pb-Bi eutectic with varying oxygen concentration (~10^{-6} – ~10^{-9} mass% O) for 10,000 h. After exposure, the solidified Pb-Bi was chemically removed from the sample surface.

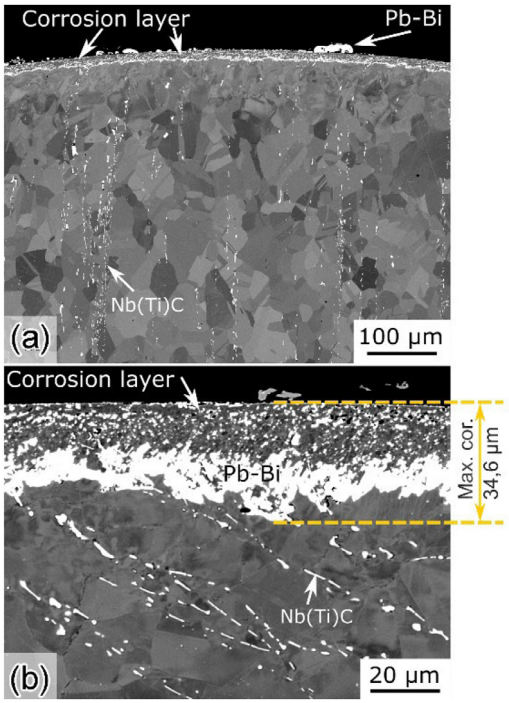

Fig. 8. Back-scattered electron images of cross-sections showing (a) in general and (b) the details of the uniform corrosion layer formed on the surface of Fe-14Cr-12Ni-10Mn-3Cu-2.5Al-1Nb steel exposed at 500 °C to static Pb-Bi eutectic with varying oxygen concentrations (~10^{-6} – ~10^{-9} mass% O) for 10000 h. Detailed structure of the corrosion zone with maximum depth of dissolution attack reaching 34.6 μm.

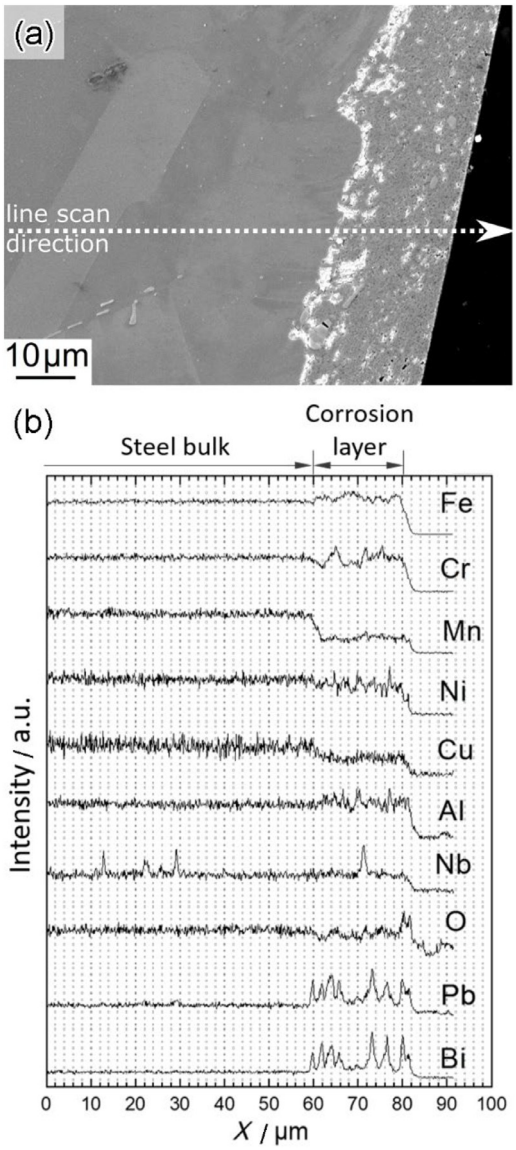

Fig. 9. Concentration profiles for different elements through the corrosion zone and near-surface steel matrix not affected by corrosion: (a) back-scattered electron image of near-surface zone of steel with formed corrosion layer, (b) concentration profiles of different elements obtained along the horizontal dotted line showed in Fig. 9(a).

shown in Fig. 12(c). The corrosion intact sections are still protected by an Al-rich oxide layer. This is confirmed by the evident Al and O peaks observed on the surface in Fig. 12(c). The mean thickness of the oxide coating is 36±6 nm (Fig. 12(d)).

Vermicular nodular oxides were detected on non-corroded areas of the sample (Fig. 13) in addition to very thin oxide films (Fig. 12(d)) and thick scales (Fig. 11). Oxide belts were observed to be arranged parallel to each other and aligned with the turning marks (Fig. 13(a)). These belts consist of agglomerates of faceted oxide crystallites mainly composed of Fe and Mn (mass fraction, %: 50.2Fe-36.0Mn-3.7Cr-1.3Ni-1.5Sn-7.1O) (Fig. 13(b, d)). Similar vermicular and nodular oxides were observed on the surface of Fe-14Cr-5Mn-12Ni-3Cu-2.5Al steel during test conducted under the same conditions [33]. Initially, re-precipitation of leached components was excluded since it should have a more random character and not be associated with the machined surface pattern of the sample. However, the clear interface between the thin oxide film and the oxide nodule (Fig. 13(c, e)) may support the reprecipitation hypothesis regarding the formation of vermicular and nodular oxides. The presence of Sn, a common impurity of Pb and Bi also supports the latter hypothesis. Normally, the formation of oxide nodules (protrusions) is associated with internal oxidation of the steel, which was not observed in our case (see Fig. 13(e)). This observation further supports the idea that the reprecipitation mechanism is responsible for the formation of nodules.

4. Discussion

In our recent paper, we have shown that AFA steels moderately alloyed by Mn (2% to 5%, mass fraction) are promising candidates for use in contact with Pb-Bi eutectics due to the exceptional durability of the oxide films formed in-situ [33]. In contrast, high-Mn (10%, mass fraction) Al-alloyed austenitic steel tested under the same conditions showed dissolution corrosion (this work). We believe that particularly in the case of high-Mn steel, manganese affects negatively the protective properties of the in-situ formed oxide layer. In this view, the dual role of Mn(Cr) as a steel constituent, which on the one hand has a very high affinity for oxygen, but on the other hand also has a high solubility in Pb-Bi, leads to the formation of large oxide agglomerates in the liquid metal in the immediate vicinity to the corroded sample surface (Fig. 11) and most-probably in the bulk of liquid metal. In this case, oxygen dissolved in the liquid metal, acts as an active trap for the dissolved steel constituents, such as Mn and Cr, by forming oxides. This process maintains the concentration mass exchange even in an isothermal system. On the contrary, in an oxygen-free isothermal system, the dissolution of Mn and Cr stops once the saturation limit of these elements in the liquid metal is reached. In other words, oxygen removes the dissolved elements of steel from the liquid solution, thereby maintaining the driving force of corrosion dissolution process, which is the difference in chemical potential in the system.

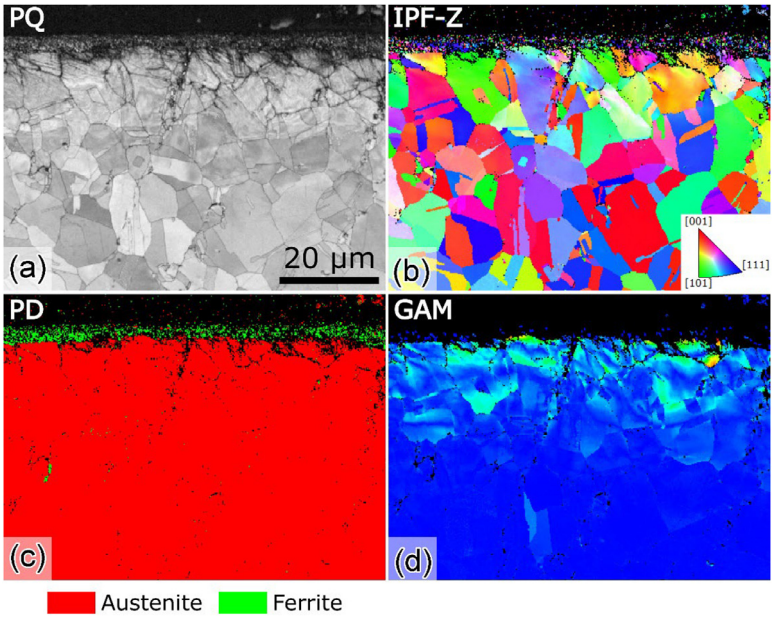

Fig. 10. EBSD maps obtained from the near-surface zone of steel with corrosion layer at the top: (a) pattern quality map (PQ); (b) inverse pole figure map (IPF-Z); (c) phase distribution map (PD); (d) grain average misorientation map (GAM) with colors showing orientation changes from 0° (blue) to 5° (red).

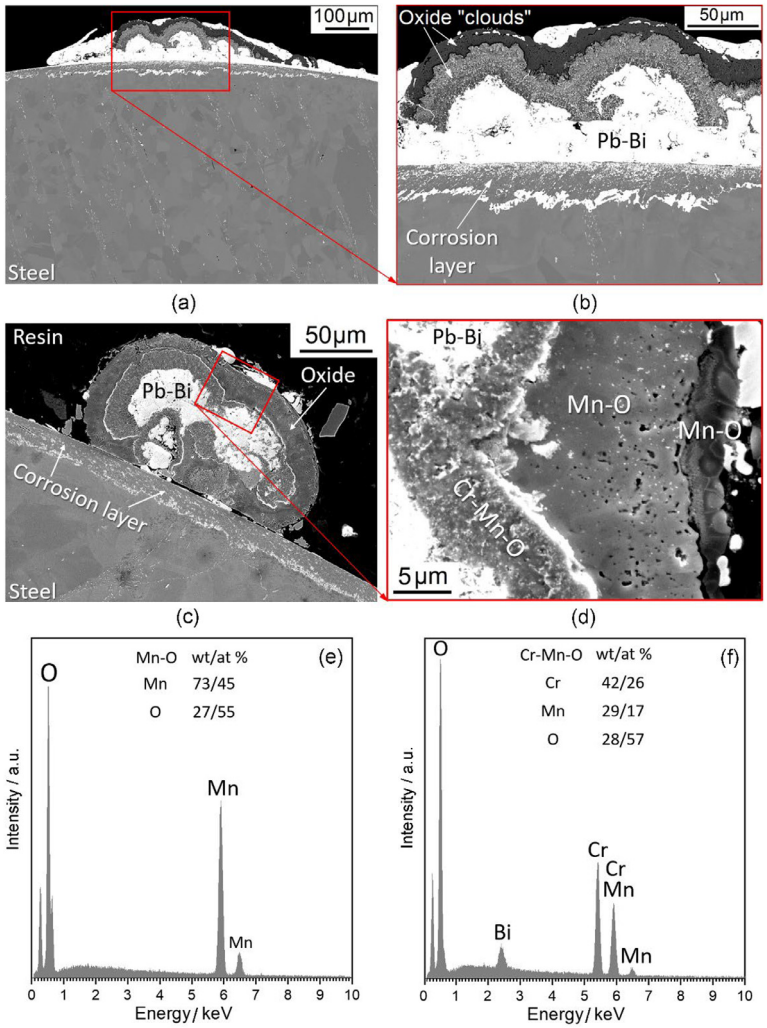

Fig. 11. Precipitates observed above the corrosion zone formed on the Fe-14Cr-12Ni-10Mn-3Cu-2.5Al-1Nb steel exposed at 500 °C to static Pb-Bi eutectic with varied oxygen concentration (~10^{-6} – ~10^{-9} mass% O) for 10000 h: (a–d) back-scattered electron images revealing general and detailed morphology, (e, f) composition of oxide precipitates.

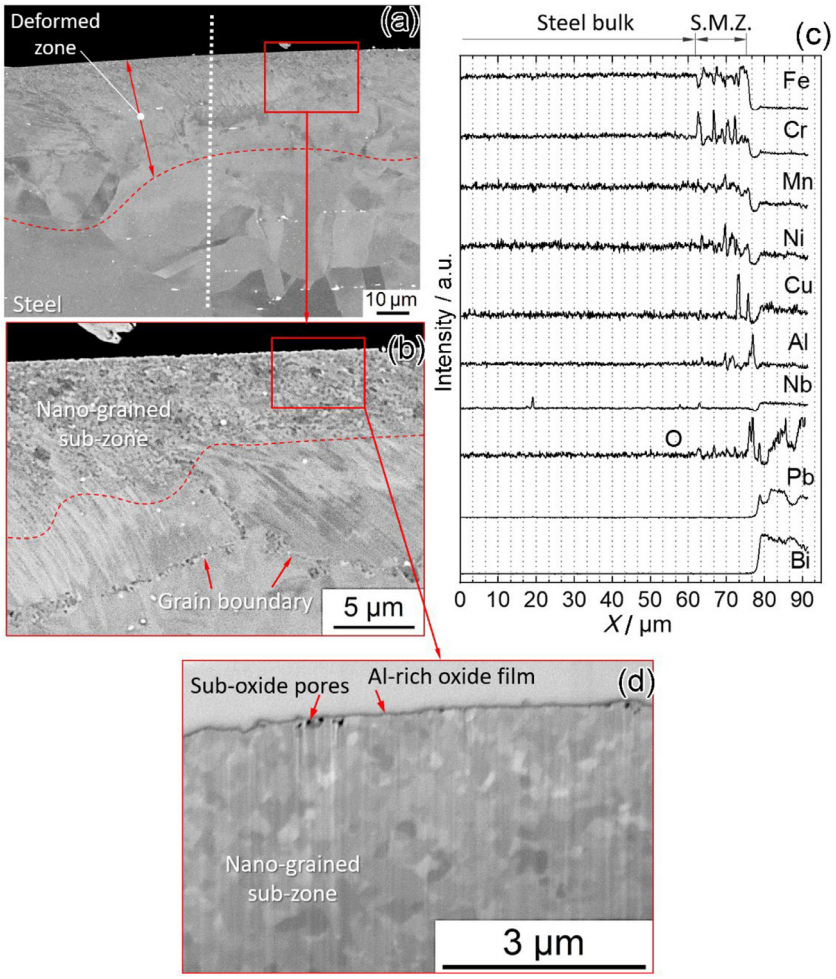

Fig. 12. Morphology and composition of not-corroded near-surface zones observed on the transversal cross-sections of the cylindrical sample of Fe-14Cr-12Ni-10Mn-3Cu-2.5Al-1Nb steel after exposure at 500 °C in static Pb-Bi eutectic for 10000 h: (a, b, d) back-scattered electron images; (c) concentration profile of elements in the near-surface zone along the white vertical dotted line shown in Fig. 12(a); S.M.Z. – Structurally-Modified near-surface Zone.

The phenomenon of formation of oxides at some distance from the site of the element solution was also observed in a few works and discussed [5,41–44]. Thus, needle-like Cr-based oxides were detected close to the dissolution affected zone formed at 450 °C on the surface of 316 L steel after exposure to static Pb-Bi with 10^{-7} mass% O [41]. In these studies, it was underlined that the found oxides are formed as a result of oxidation of the initially dissolved Cr. Schroer also reported re-precipitation of dissolved Cr in the view of Cr-based oxide layer at some distance from the surface of Ni-Cr alloy at 750 °C in static Pb with 10^{-6} mass% dissolved oxygen after 120 h [42].

Summarizing our observations and literature data, the phenomenological mechanism of interaction of high-Mn austenitic steel with Pb-Bi[O] includes the following main steps: leaching of Ni, Mn and Cr by the liquid Pb-Bi eutectic; reaction of dissolved Mn and Cr with O dissolved in liquid metal followed by re-precipitation of reaction products in the view of the Mn-Cr oxide that stimulates further leaching of steel constituents. Dissolved Ni remains in a liquid solution since the oxygen concentration in the liquid metal is too low to provide the formation of $NiO_{(s)}$ (Fig. 3). The overall corrosion process might be named as an oxygen-driven de-alloying of steel constituents by liquid metal.

Generalizing the obtained results we would like to remind you that the initial idea of adding oxygen into liquid metals like Pb and Pb-Bi eutectic lies in the formation of protective and continuous oxide layer in-situ on the steel surface [7]. The obtained results imply that this task becomes complicated when the material is alloyed with comparable high amounts of Mn and Cr which behave ambivalently i.e., are apt to dissolution followed by the oxidation in the liquid metal [5] which result in oxygen-driven de-alloying of steel constituents by the liquid metal.

Since our investigation focused on the long-term test, it can be assumed that the initially formed oxide layer started to fail locally when we changed the oxygen concentration from oxidizing to dissolving mode. In 80% of the cases, the degradation of the oxide layer results in the start and propagation of dissolution. However, some areas (20%) of the steel surface are still protected from dissolution by the Al-rich oxide layer. It is expected that with time these areas will eventually disappear and the entire surface will exhibit dissolution corrosion. Once the dissolution process begins, it is unlikely that oxide films will be able to re-form on the corroded surface. On the other hand, it can be also assumed that most of the areas from the beginning of the contact with liquid metal tend to oxidize, while other areas tend to dissolve due to local inhomogeneities on the solid surface (structural and compositional) and/or from the side of the liquid metal (variations in oxygen concentration). Short-term tests should be conducted to investigate the expressed suppositions and elucidate the initial and intermediate stages of the evolution of oxide film composition. This will improve our understanding of potential self-healing or degradation phenomena related to the in-situ formed oxide films.

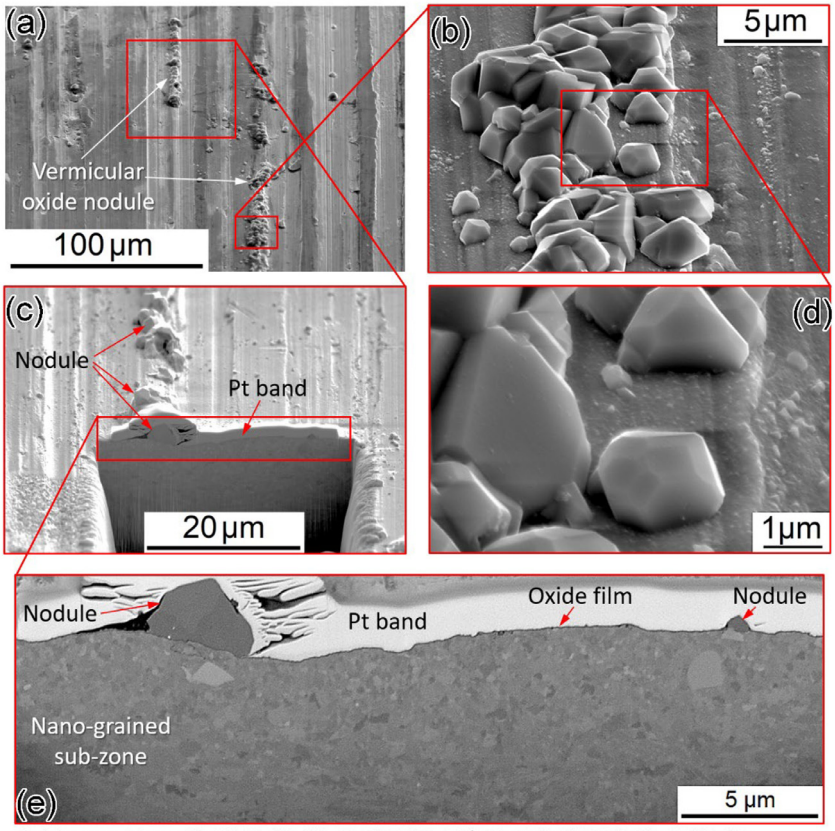

Fig. 13. Surface and sub-surface zones morphology in the vicinity of vermicular nodular oxides formed on Fe-14Cr-12Ni-10Mn-3Cu-2.5Al-1Nb steel at 500 °C in static Pb-Bi eutectic for 10000 h: (a) general view of surface with vermicular nodular oxide belts, (b) detailed view of agglomerates of faceted oxide crystallites compousing vermicular nodular oxides belts, (c) focused ion beam created trench, (d) detailed view of faceted oxide crystallites, (e) metallographic cross-section showing detailed structure and morphology of near-surface zones of steel consisting of: top oxide nodules; thin oxide film and sub-oxide nano-grained zone of steel matrix. Sample is cleaned chemically with respect to solidified Pb-Bi.

5. Conclusions

The long-term corrosion behavior of the high-Mn Al-alloyed Fe-14Cr-12Ni-10Mn-3Cu-2.5Al-1Nb austenitic steel in static Pb-Bi eutectic was investigated by performing a 10000 h corrosion test at 500 °C. The concentration of dissolved oxygen was varied during the course of the test from ~10^{-6} to ~10^{-9} mass% to ensure subsequent periods of oxidation and dissolution interaction modes, respectively. The following conclusions can be drawn from the results obtained:

- The steel underwent oxygen-driven de-alloying, resulting in:
  - Formation of a near-surface ferrite corrosion zone penetrated by Pb and Bi and depleted in Mn, Ni, Cu, Cr and to a lower extent in Fe;
  - Reprecipitation of dissolved Mn and Cr at the sample surface in the form of layered oxides;
  - The average depth of corrosion is 15±4 µm and the maximum depth locally reached is about 35 µm;
- The high-Mn Al-alloyed steel Fe-14Cr-12Ni-10Mn-3Cu-2.5Al-1Nb exhibited dissolution corrosion in contrast to steels moderately alloyed by Mn (2% to 5%, mass fraction) with nearly similar aluminium content Fe-14Cr-2Mn-20Ni-0.5Cu-3Al and Fe-14Cr-5Mn-12Ni-3Cu-2.5Al which showed protective oxidation under the same test conditions.

Declaration of competing interest

The authors declare that they have no known competing financial interests or personal relationships that could have appeared to influence the work reported in this paper.

CRediT authorship contribution statement

Valentyn Tsisar: Conceptualization, Data curation, Formal analysis, Investigation, Methodology, Validation, Visualization, Writing – original draft, Writing – review & editing. **Erich Stergar:** Conceptualization, Data curation, Formal analysis, Funding acquisition, Investigation, Project administration, Resources, Supervision, Writing – review & editing. **Serguei Gavrilov:** Conceptualization, Data curation, Formal analysis, Investigation, Methodology, Project administration, Resources, Supervision, Validation, Writing – review & editing. **Eloa Lopes Maia:** Data curation, Formal analysis, Investigation, Visualization, Writing – review & editing. **Wouter Van Renterghem:** Formal analysis, Validation, Visualization, Writing – review & editing. **Pierre Louette:** Data curation, Formal analysis, Visualization. **Stéphane Lucas:** Data curation, Formal analysis, Visualization.

Acknowledgments

The investigations performed in the framework of the ongoing program of characterization of compatibility of candidate materials with liquid Pb-Bi eutectic for development of the accelerator driven system MYRRHA. The research leading to these results is partially funded by the European Commission HORIZON 2020 Framework Programme under grant agreement No 755269. The authors are very thankful to Mr. Michael P. Brady (Materials Science and Technology Division, Oak Ridge National Lab, Oak Ridge, TN 37831-6115, USA) for supplying AFA steels. The authors would like to thank for the technical support to Mr. Joris Jasper, Mr. Yves Florenty, Mr. Bart Geyskens and Mr. Jelle Bouwens (SCK.CEN).

References

[1] J. Zhang, Liquid Metal Corrosion: Fundamental Theory and Applications, Woodhead Publishing, an imprint of Elsevier, Cambridge, MA, 2023.

[2] X. Gong, M.P. Short, T. Auger, E. Charalampopoulou, K. Lambrinou, Environmental degradation of structural materials in liquid lead- and lead-bismuth eutectic-cooled reactors, Prog. Mater. Sci. 126 (2022) 100920.

[3] NEAHandbook On Lead-bismuth Eutectic Alloy and Lead Properties, Materials Compatibility, Thermal-hydraulics and Technologies –2015 Edition, OECD Publishing, Paris, 2024.

[4] F. Balbaud, L. Martinelli, 22 - Corrosion issues in lead-cooled fast reactor (LFR) and accelerator driven systems (ADS), in: D. Féron (Ed.), Nuclear Corrosion Science and Engineering, Ed., Woodhead Publishing, Cambridge, Philadelphia (Pa, 2012, pp. 807–841.

[5] C. Schroer, O. Wedemeyer, J. Novotny, A. Skrypnik, J. Konys, Selective leaching of nickel and chromium from Type 316 austenitic steel in oxygen-containing lead–bismuth eutectic (LBE), Corros. Sci. 84 (2014) 113–124.

[6] F. Balbaud-Célérier, J.-L. Courouau, D. Féron, L. Martinelli, F. Rouillard, Corrosion of structural materials by liquid metals used in fusion, fission, and spallation, in: S. Ritter (Ed.), Nuclear Corrosion: Research, Progress and Challenges, Ed., Woodhead Publishing, 2020, pp. 437–457.

[7] A.E. Rusanov, B.A. Shmatko, Oxide protection of materials in melts of lead and bismuth, Mater. Sci. 36 (2000) 689–700.

[8] V. Tsisar, C. Schroer, O. Wedemeyer, A. Skrypnik, J. Konys, Corrosion behavior of austenitic steels 1.4970, 316L and 1.4571 in flowing LBE at 450 and 550 °C with 10−7mass% dissolved oxygen, J. Nucl. Mater. 454 (2014) 332–342.

[9] V. Tsisar, C. Schroer, O. Wedemeyer, A. Skrypnik, J. Konys, Long-term corrosion of austenitic steels in flowing LBE at 400 °C and 10−7 mass% dissolved oxygen in comparison with 450 and 550°C, J. Nucl. Mater. 468 (2016) 305–312.

[10] C. Schroer, O. Wedemeyer, J. Novotny, A. Skrypnik, J. Konys, Long-term service of austenitic steel 1.4571 as a container material for flowing lead–bismuth eutectic, J. Nucl. Mater. 418 (2011) 8–15.

[11] C. Schroer, J. Konys, Quantification of the long-term performance of steels T91 and 316L in oxygen-containing flowing lead-bismuth eutectic at 550 °C, J. Eng. Gas Turbines Power 132 (2010) 82901.

[12] L. Kosek, L. Rozumova, A. Hojna, C. Aparicio, M. Vronka, J. Vit, Mechanism of localized corrosion issues of austenitic steels exposed to flowing lead with 10−7 wt.% oxygen at 480 °C up to 16000 h, J. Nucl. Mater. 572 (2022) 154045.

[13] M.P. Brady, Y. Yamamoto, M.L. Santella, P.J. Maziasz, B.A. Pint, C.T. Liu, Z.P. Lu, H. Bei, The development of alumina-forming austenitic stainless steels for high-temperature structural use, JOM 60 (2008) 12–18.

[14] M.P. Brady, G. Muralidharan, Y. Yamamoto, B.A. Pint, Development of 1100 °C capable alumina-forming austenitic alloys, Oxid. Met. 87 (2017) 1–10.

[15] Y. Yamamoto, M.P. Brady, M.L. Santella, H. Bei, P.J. Maziasz, B.A. Pint, Overview of strategies for high-temperature creep and oxidation resistance of alumina-forming austenitic stainless steels, Metall. Mater. Trans. A 42 (2011) 922–931.

[16] M.P. Brady, J. Magee, Y. Yamamoto, D. Helmick, L. Wang, Co-optimization of wrought alumina-forming austenitic stainless steel composition ranges for high-temperature creep and oxidation/corrosion resistance, Mater. Sci. Eng. A 590 (2014) 101–115.

[17] N.M. Yanar, B.S. Lutz, L. Garcia-Fresnillo, M.P. Brady, G.H. Meier, The effects of water vapor on the oxidation behavior of alumina forming austenitic stainless steels, Oxid. Met 84 (2015) 541–565.

[18] V. Tsisar, Z.J. Zhou, O. Wedemeyer, A. Skrypnik, C. Schroer, Effect of oxygen concentration in static Pb-Bi eutectic on corrosion mode of aluminum-alloyed austenitic steels at 550 °C for 1000 h, Mater. Sci. Forum 1024 (2021) 79–85.

[19] H. Shi, A. Jianu, A. Weisenburger, C. Tang, A. Heinzel, R. Fetzer, F. Lang, R. Stieglitz, G. Müller, Corrosion resistance and microstructural stability of austenitic Fe–Cr–Al–Ni model alloys exposed to oxygen-containing molten lead, J. Nucl. Mater. 524 (2019) 177–190.

[20] J. Ejenstam, P. Szakálos, Long term corrosion resistance of alumina forming austenitic stainless steels in liquid lead, J. Nucl. Mater. 461 (2015) 164–170.

[21] L. Shen, G. Cao, D. Lang, H. Peng, Y. Wen, Fe-14Ni-14Cr-2.5Al steel showing excellent corrosion-resistance in flowing LBE at 550 °C and high temperature strength, J. Nucl. Mater. 587 (2023) 154703.

[22] F.H. Stott, G.C. Wood, J. Stringer, The influence of alloying elements on the development and maintenance of protective scales, Oxid. Met. 44 (1995) 113–145.

[23] C. Schroer, O. Wedemeyer, J. Konys, Aspects of minimizing steel corrosion in liquid lead-alloys by addition of oxygen, Nucl. Eng. Des. 241 (2011) 4913–4923.

[24] A.L. Marasco, D.J. Young, The oxidation of iron-chromium-manganese alloys at 900 °C, Oxid. Met. 36 (1991) 157–174.

[25] X. Xu, X. Zhang, X. Sun, Z.P. Lu, Roles of Manganese in the High-temperature Oxidation Resistance of Alumina-forming Austenitic Steels at above 800 °C, Oxid. Met. 78 (2012) 349–362.

[26] Y. Yamamoto, M.L. Santella, C.T. Liu, N.D. Evans, P.J. Maziasz, M.P. Brady, Evaluation of Mn substitution for Ni in alumina-forming austenitic stainless steels, Mater. Sci. Eng. A 524 (2009) 176–185.

[27] Y. Zhao, P. Chen, W. Wen, Y. Deng, K. Peng, Y. Liu, Effect of Mn content on the high-temperature oxidation behaviors of Mn-substituted-for-Ni alumina-forming austenitic stainless steel, J. Mater. Res. Technol. 26 (2023) 7816–7828.

[28] H. Wang, H. Yu, S. Kondo, N. Okubo, R. Kasada, Corrosion behaviour of Al-added high Mn austenitic steels in molten lead bismuth eutectic with saturated and low oxygen concentrations at 450 °C, Corros. Sci. 175 (2020) 108864.

[29] H. Wang, H. Yu, J. Liu, S. Kondo, N. Okubo, R. Kasada, Characterization and corrosion behavior of Al-added high Mn ODS austenitic steels in oxygen-saturated lead–bismuth eutectic, Corros. Sci. 209 (2022) 110818.

[30] C. Schroer, V. Koch, O. Wedemeyer, A. Skrypnik, J. Konys, Silicon-containing ferritic/martensitic steel after exposure to oxygen-containing flowing lead–bismuth eutectic at 450 and 550 °C, J. Nucl. Mater. 469 (2016) 162–176.

[31] Y. Kurata, Corrosion behavior of Si-enriched steels for nuclear applications in liquid lead–bismuth, J. Nucl. Mater. 437 (2013) 401–408.

[32] B.A. Pint, Y.-F. Su, M.P. Brady, Y. Yamamoto, J. Jun, M.R. Ickes, Compatibility of alumina-forming austenitic steels in static and flowing Pb, JOM 73 (2021) 4016–4022.

[33] V. Tsisar, E. Stergar, S. Gavrilov, W. van Renterghem, P. Louette, S. Lucas, Effect of variation in oxygen concentration in static Pb–Bi eutectic on long-term corrosion performance of Al-alloyed austenitic steels at 500 °C, Corros. Sci. 195 (2022) 109963.

[34] J. Lim, G. Manfredi, K. Rosseel, A. Aerts, Performance of electrochemical oxygen pump in a liquid lead-bismuth eutectic loop, J. Electrochem. Soc. 166 (2019) E153–E158.

[35] G. Manfredi, J. Lim, K. Rosseel, J. Van den Bosch, T. Doneux, C. Buess-Herman, A. Aerts, Comparison of solid metal–metal oxide reference electrodes for potentiometric oxygen sensors in liquid lead–bismuth eutectic operating at low temperature ranges, Sens. Actuators B Chem. 214 (2015) 20–28.

[36] J. Lim, A. Mariën, K. Rosseel, A. Aerts, J. Van den Bosch, Accuracy of potentiometric oxygen sensors with Bi/Bi2O3 reference electrode for use in liquid LBE, J. Nucl. Mater. 429 (2012) 270–275.

[37] G.C. Allen, S.J. Harris, J.A. Jutson, J.M. Dyke, A study of a number of mixed transition metal oxide spinels using X-ray photoelectron spectroscopy, Appl. Surf. Sci. 37 (1989) 111–134.

[38] M.C. Biesinger, B.P. Payne, A.P. Grosvenor, L.W. Lau, A.R. Gerson, R.S. Smart, Resolving surface chemical states in XPS analysis of first row transition metals, oxides and hydroxides: cr, Mn, Fe, Co and Ni, Appl. Surf. Sci. 257 (2011) 2717–2730.

[39] M.A. Langell, J.G. Kim, D.L. Pugmire, W. McCarroll, Nature of oxygen at rocksalt and spinel oxide surfaces, J. Vac. Sci. Technol. A-Vac. Surf. Films 19 (2001) 1977–1982.

[40] O. Yeliseyeva, V. Tsisar, G. Benamati, Influence of temperature on the interaction mode of T91 and AISI 316L steels with Pb–Bi melt saturated by oxygen, Corros. Sci. 50 (2008) 1672–1683.

[41] O. Klok, K. Lambrinou, S. Gavrilov, J. Lim, I. de Graeve, Effect of lead-bismuth eutectic oxygen concentration on the onset of dissolution corrosion in 316 L austenitic stainless steel at 450 °C, J. Nucl. Eng. Rad. Sci. 4 (2018) 031019.

[42] C. Schroer, Fundamental Interactions of Steels and Nickel-based Alloys with Lead--based Liquid Alloys or Liquid Tin, in: TMS 2021 150th Annual Meeting & Exhibition Supplemental Proceedings, Ed., Springer, Cham, 2021, pp. 642–656.

[43] C. Schroer, Dissimilar metal solution from solid alloys as observed for steels and nickel-based alloys in the presence of lead-based liquid alloys or liquid tin, JOM 73 (2021) 4000–4008.

[44] C. Schroer, A. Skrypnik, O. Wedemeyer, J. Konys, Oxidation and dissolution of iron in flowing lead–bismuth eutectic at 450 °C, Corros. Sci. 61 (2012) 63–71.